

Article

Identification of Radioactive Mineralized Lithology and Mineral Prospectivity Mapping Based on Remote Sensing in High-Latitude Regions: A Case Study on the Narsaq Region of Greenland

Li He ^{1,2,*}, Pengyi Lyu ^{1,3,*}, Zhengwei He ^{1,3}, Jiayun Zhou ⁴, Bo Hui ⁴, Yakang Ye ⁴, Huilin Hu ³, Yanxi Zeng ³ and Li Xu ^{3,4}

- ¹ State Key Laboratory of Geohazard Prevention and Geoenvironment Protection, Chengdu University of Technology, Chengdu 610059, China; hzw@cdut.edu.cn
- ² College of Tourism and Urban-Rural Planning, Chengdu University of Technology, Chengdu 610059, China
- ³ College of Earth Sciences, Chengdu University of Technology, Chengdu 610059, China; abbey.wang@onestopwarehouse.com.au (H.H.); cissy.zengxixi@sina.com (Y.Z.); xulicdzhs@163.com (L.X.)
- ⁴ Institute of Multipurpose Utilization of Mineral Resources, China Geological Survey, Chengdu 610041, China; zhszy@aliyun.com (J.Z.); huibo0728@foxmail.com (B.H.); yeyakang920617@sina.cn (Y.Y.)
- * Correspondence: heli2020@cdut.edu.cn (L.H.); davislpy1045@gmail.com (P.L.)



Citation: He, L.; Lyu, P.; He, Z.; Zhou, J.; Hui, B.; Ye, Y.; Hu, H.; Zeng, Y.; Xu, L. Identification of Radioactive Mineralized Lithology and Mineral Prospectivity Mapping Based on Remote Sensing in High-Latitude Regions: A Case Study on the Narsaq Region of Greenland. *Minerals* **2022**, *12*, 692. <https://doi.org/10.3390/min12060692>

Academic Editor: Amin Beiranvand Pour

Received: 17 May 2022

Accepted: 27 May 2022

Published: 30 May 2022

Publisher's Note: MDPI stays neutral with regard to jurisdictional claims in published maps and institutional affiliations.



Copyright: © 2022 by the authors. Licensee MDPI, Basel, Switzerland. This article is an open access article distributed under the terms and conditions of the Creative Commons Attribution (CC BY) license (<https://creativecommons.org/licenses/by/4.0/>).

Abstract: The harsh environment of high-latitude areas with large amounts of snow and ice cover makes it difficult to carry out full geological field surveys. Uranium resources are abundant within the Ilimaussaq Complex in the Narsaq region of Greenland, where the uranium ore body is strictly controlled by the Lujavrite formation, which is the main ore-bearing rock in the complex rock mass. Further, large aggregations of radioactive minerals appear as thermal anomalies on remote sensing thermal infrared imagery, which is indicative of deposits of highly radioactive elements. Using a weight-of-evidence analysis method that combines machine-learned lithological classification information with information on surface temperature thermal anomalies, the prediction of radioactive element-bearing deposits at high latitudes was carried out. Through the use of Worldview-2 (WV-2) remote sensing images, support vector machine algorithms based on texture features and topographic features were used to identify Lujavrite. In addition, the distribution of thermal anomalies associated with radioactive elements was inverted using Landsat 8 TIRS thermal infrared data. From the results, it was found that the overall accuracy of the SVM algorithm-based lithology mapping was 89.57%. The surface temperature thermal anomaly had a Spearman correlation coefficient of 0.63 with the total airborne measured uranium gamma radiation. The lithological classification information was integrated with surface temperature thermal anomalies and other multi-source remote sensing mineralization elements to calculate mineralization-favorable areas through a weight-of-evidence model, with high-value mineralization probability areas being spatially consistent with known mineralization areas. In conclusion, a multifaceted remote sensing information finding method, focusing on surface temperature thermal anomalies in high-latitude areas, provides guidance and has reference value for the exploration of potential mineralization areas for deposits containing radioactive elements.

Keywords: high latitudes; weak information; thermal anomalies; radioactive element deposits

1. Introduction

High-latitude regions lie between the 60° north and 60° south latitudes to the north and south poles of the Earth's surface, respectively, and receive the least solar radiation. Therefore, the climate is cold, and most areas are covered in snow and ice for long periods, which makes it difficult to carry out comprehensive geological field surveys. With remote sensing technology, it is possible to overcome the time constraints of field investigations and

select multiple sources of remote sensing data for long time series analysis. Spectroscopic information from remote sensing can screen the diversity of the mineral spectrum, which depends on the physical interactions of electrons and molecular structures within the material [1–3]. Multispectral data and wave spectrum identification algorithms have made it possible for remote sensing technology to predict mineralized target areas [4–12]. The identification of the lithology based on remote sensing data automatically classified by computers can help quickly obtain geological background information of the target area in comparison to the long cycle time of a geological field survey. Lithological classification via machine learning not only fully utilizes the spectral and rock texture features among different rocks but also improves the lithological classification accuracy [13–20].

The Gardar igneous intrusions in southern Greenland are typically high in alkali elements, such as sodium, whereas the Ilimaussaq Complex, which was formed later in the magmatic intrusion system, has a high concentration of rare and radioactive elements [21,22]. Owing to the enrichment of radioactive elements, such as uranium and thorium, the earth heat flow generated will inevitably cause the enriched areas to exhibit extreme radioactivity; this radioactive heat can be detected by surface thermal anomalies [23–26]. Information on surface thermal anomalies can be obtained in various ways, and thermal infrared remote sensing technology is a widely used technique. Based on the information obtained from thermal anomalies, it is possible to interpret certain topographic changes (basement uplift and depression), volcanoes, hot springs, faults, etc. [27]. The use of thermal infrared remote sensing technology for geothermal resources has made it easier to develop resource-prospecting techniques. In the field of geology, this technology has been applied for decades, and it is widely used in large-scale geothermal resource surveys, mountain surveys, volcano early-warning systems, and earthquake prediction [28–32]. The introduction of remote sensing data, such as ASTER and Landsat TIRS, effectively increases the diversity of surface temperature inversion and more effectively traces radioactive minerals and geothermal resources, playing an important role in the field of geological and mineral exploration [33–37].

This paper aims to identify radioactive element enrichment areas and ore-bearing lithologies by remote sensing techniques and to study a method for predicting the favorability of mineralization of radioactive deposits at high latitudes using a weight-of-evidence model. The inversion of surface thermal anomalies from thermal infrared remote sensing data is conducted in the harsh Greenland Narsaq region, where areas of radioactive mineral enrichment are extracted. Machine learning techniques are also used to identify and classify regional lithologies enriched in radioactive elements. The integration of multi-source remote sensing information using the Weight of Evidence model can be effective in conducting mineral resource surveys in high latitude regions.

2. Study Area

2.1. Physical Geography

The study area is in the Narsaq region of Gardar Province in southern Greenland, ranging from 44°30′ to 46°30′ W in longitude and 60°45′ to 61°20′ N in latitude. The region has very few land-based road systems due to the extremely large number of bays (Figure 1). The region experiences a polar climate, with the average temperature in winter (January) being −6 °C, while the average temperature during the coastal summer (July) is 7 °C, with July and August having the highest temperatures of the year.

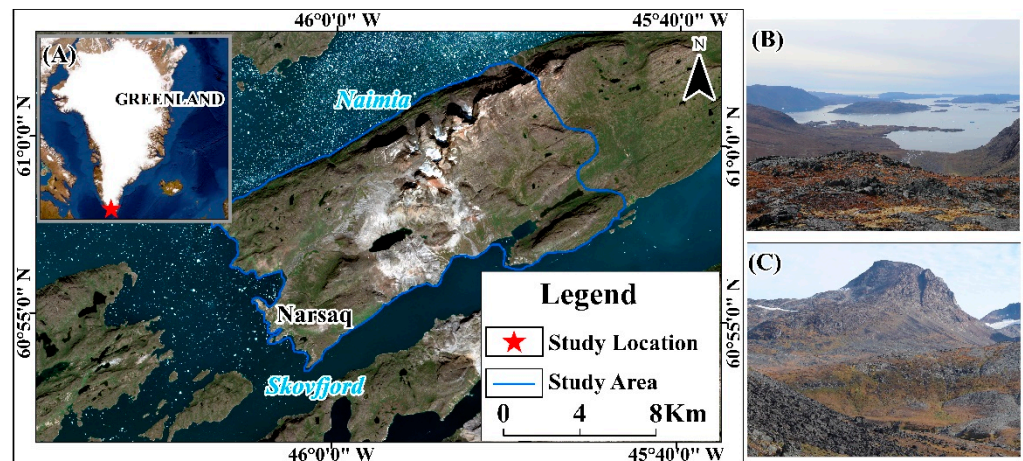


Figure 1. (A) Location map based on Sentinel-2's true color 432 band combinations; (B,C) A realistic view of the study area environment.

2.2. Geological Background

The geological setting of the study area is dominated by the southern parts of the Palaeo-Craton and the Palaeoproterozoic Ketilidian orogenic belts. The Mesoproterozoic Gardar igneous province crosses the Ketilidian orogenic belt. The province of Gardar is marked by the development of deposits of faulted, clastic, and volcanic rocks with high alkaline magmatic activity. The Gardar intrusive complex is dominated by differentiated silica-alumina rocks, including syenite, nepheline syenite, quartz syenite, and granite. Giant vein rocks are dominated by weakly alkaline gabbro and syenite gabbro, with faults developing parallel to rift valleys in formations affected by lithosphere stretching [38]. Within the Julianehab Granite, there are several east–northeast (NEE) oriented fault planes, where the lateral displacement along the fault planes is uncertain, but the vertical displacement is evident. The displacement faults incorporate NEE to north–east (NE) trending sinistral faults, as well as north–north–west (NNW) to north–north–east (NNE) trending r-dextral faults, forming conjugate faults (Figure 2) [22,39,40].

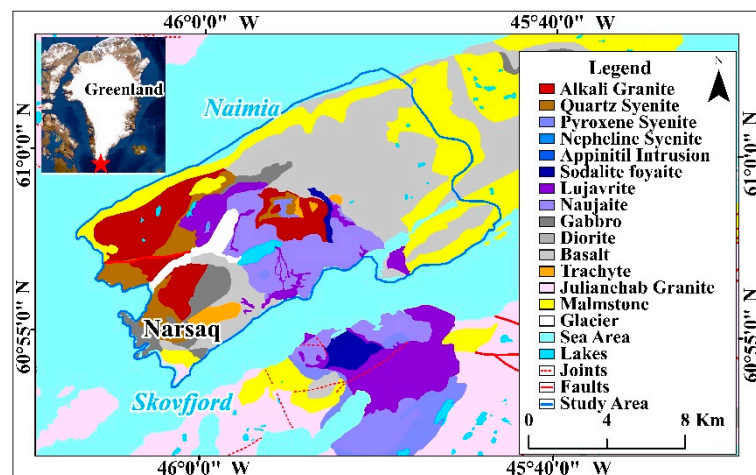


Figure 2. Geological map of the study area.

3. Material and Methods

3.1. Data and Pre-Processing

Several data sources were applied to meet the needs of the study (Table 1), including the following:

1. Visible light near the infrared (NIR) data of the Sentinel-2AB (S2AB) satellite;
2. Thermal infrared data of LANDSAT-8TIRS (LTRS) satellite;

3. Visible light near the infrared data of the Worldview-2 (WV-2) satellite;
4. ASTER GDEM 30 m spatial resolution ground elevation model data;
5. Measured data of the SVC HR-1024i full-spectrum ground object spectrometer.

Table 1. List of data used.

Data Type	Maximum Spatial Resolution (m)	Acquisition Time
Worldview-2	0.5	29 August 2017
Landsat 8 TIRS	15	29 July 2018, 7 August 2018, 26 August 2019
Sentinel-2	10	10 August 2019, 6 April 2020
ASTER GDEM V3	30	August 2019
SVC HR-1024i	-	July 2019

3.1.1. Visible NIR Remote Sensing Data

The visible NIR satellite remote sensing data were selected from S2AB and WV-2 satellite data. Among these, the main payload of the Sentinel satellite is the Multi-Spectral Imager (MSI), operating in the visible, near-infrared, and short-wave infrared spectral bands, with ground resolutions of 10 m, 20 m, and 60 m, respectively [41,42]. The WV-2 satellite is a high spatial resolution satellite data, capable of providing panchromatic images at 0.46 m and multispectral images at 1.8 m resolutions [43].

3.1.2. Thermal Infrared Remote Sensing Data

The LTRS data were chosen as a source of thermal infrared radiation information, whose thermal infrared sensor covers two thermal infrared bands, both of which have a resolution of 100 m in the wavelength range of 10.60–12.51 μm [44,45].

3.1.3. Topographic Surface Elevation Data

Topographic data were extracted using ASTER GDEM V3, a digital elevation model acquired and released by NASA's Earth observation satellite, named Terra, with a resolution of one arc-second (30 m), covering 99% of the global land surface from 83° N to 83° S [46].

3.1.4. Field Measurements of Feature Spectral Data

Field spectra were collected using the SVC HR-1024i (SVC, Poughkeepsie, NY USA) full spectrum spectroradiometer, which has a spectral measurement range of 350–2500 nm and a total of 1024 channels. The spectral resolution is 2.8 nm in the 350–1000 nm range, 3.6 nm in the 1000–1900 nm range, and 2.5 nm in the 1900–2500 nm range.

Remote sensing data pre-processing was carried out using the ENVI software (Version 5.6, ESRI, Redlands, CA, USA) [47], which provides multi-source remote sensing data with radiometric calibration, FLAASH atmospheric correction, geometric correction, and image enhancement as remote sensing image pre-processing steps. The measured spectral information was obtained from 50 rock samples collected at the mine site, and the rock spectra were collected in a dark room environment. As the spectral features of the rocks acquired from remote sensing images come from exposed rock surfaces, which are affected by weathering and other environmental factors, the rock samples were not ground to simulate the real conditions in the field, and a total of 128 valid spectra were collected (Figure 3).

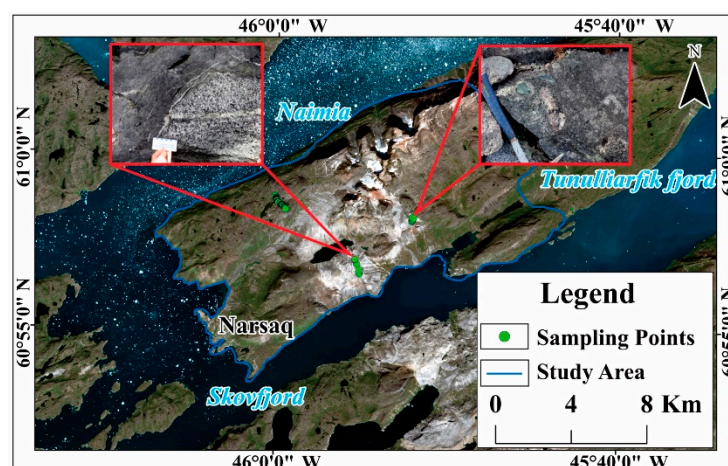


Figure 3. Distribution map of field spectral samples (the base image is a combination of the 432 bands of Sentinel-2).

3.2. Remote Sensing for Geological Background Information Extraction

The interpretation and investigation of geological background information are fundamental for the prediction of regional mineralization; during geological action, areas spatially located in geological-variation regions and marginal areas are often the sites of endogenous deposits. Significant deposits are often found at the junction of tectonic plates and are temporally associated with tectonic events, with the distribution of mineralization information roughly corresponding to the occurrence of tectonic anomalies. Furthermore, tectonics provides a good environment for the formation, storage, and transportation of deposits; the mapping of the geological base information will facilitate the understanding of the regional framework and the rapid tracing of mineralization prediction areas. Extraction was carried out from three perspectives: lithological, tectonic, and alteration information.

The interpretation of lithologies and formations in the study area was based on visual interpretation. Firstly, the ArcGIS and ENVI software were used to enhance the remote sensing image information, and the interpretability of the interpreted lithologies and structures was enhanced through optimal waveband analysis and image filtering. Directional features, which are important properties of linear constructions, were enhanced by directional filtering in the study area to identify linear constructions more intuitively. The image was enhanced using a 5 by 5 directional convolutional filtering method, and the image—after enhancement—exhibited extremely distinct linear features from north–north-east to north-east–east (45° range). Lithologies and formations smaller than the spatial resolution per image element are difficult to distinguish accurately and are often interpreted indirectly utilizing the topography, vegetation, water systems, etc.

For the extraction of alteration information, the study area used principal component analysis (PCA) based on the method proposed by Crosta scholars for the extraction of hydroxyl and iron-stained alterations. The PCA uses the multidimensional orthogonal linear variation of the interrelationships between variables, and the entire method is based on mathematical and statistical analyses. The method can reduce the dimensionality of remote sensing information, capture the spectral differences of features, and serve to enhance and compress the data while also removing correlations between information in the same region or the same remote sensing data band [48]. Secondary oxides are the most represented group of iron-stained alteration minerals, while only a small proportion of the other alteration minerals are primary. In the 2, 4, and 11 bands of Sentinel-2, the divalent and trivalent ions of iron have characteristic absorption valleys; therefore, these three bands were chosen as the main bands for iron-stained alteration extraction. Alteration minerals that contain hydroxyl or carbonate ions include chlorite and kaolinite. The spectra of the mineralized rocks have two unique features compared to the spectra of other rocks, where a slowly rising plateau forms at wavelengths of 1.0–1.4 μm , while the spectrum at

1.9–2.0 μm forms an extremely strong absorption valley, indicating absorption properties in the near-infrared band; therefore, bands 2, 8, and 12 of Sentinel-2 were chosen to extract the hydroxyl alteration.

3.3. The Support Vector Machines(SVM) Lithology Extraction Technique

SVMs are widely used in the field of geological rock identification and classification. As a method of machine learning, their core concept involves projecting data into a high-dimensional space, constructing an optimal hyperplane in the high-dimensional space, and using this optimal plane to classify different data. The object-oriented SVM classification method, which uses the object as the basic unit, is a classification method that combines multiple types of feature information, including spectrum, texture, shape, and topology information [49–52]. The method of classifying image units using SVMs (Figure 4) differs from those of other algorithms in that it minimizes a priori intervention and, therefore, presents the classification results objectively; in addition, it is efficient and stable [53,54].

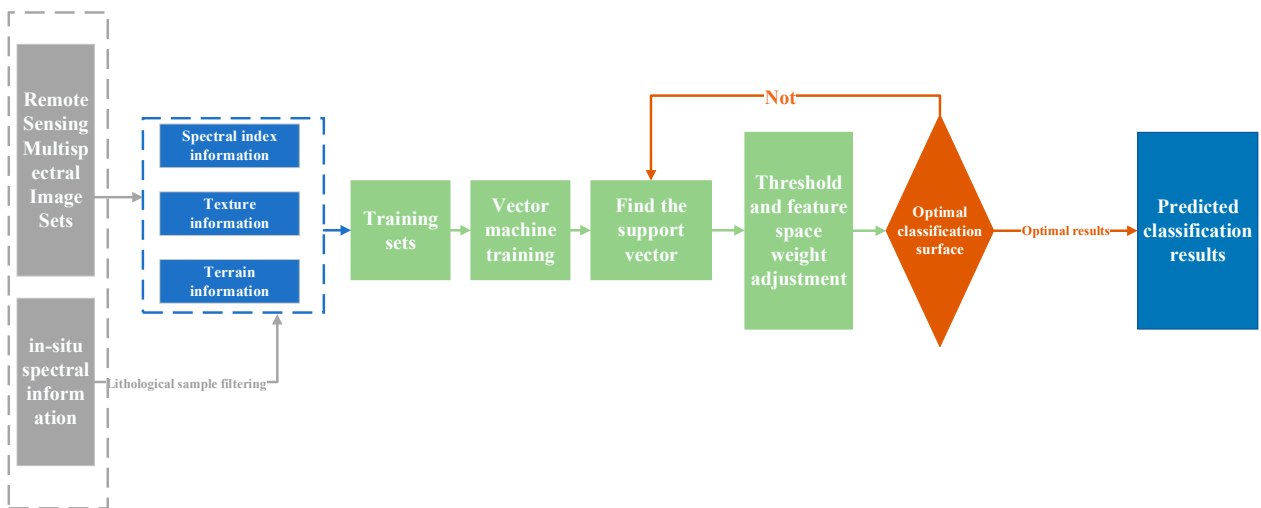


Figure 4. Support vector machine classification recognition process.

The SVM approach is considered to be a good method for classification extraction because it has high generalization performance and does not require prior knowledge, even if the dimensionality of the input space is high [55]. Intuitively, SVM algorithm extraction is based on finding a hyperplane, provided a set of points belong to either of the two classes, such that the proportion of points in the same class on the same side is maximized while also maximizing the distance between either class and the hyperplane [56] (Figure 5).

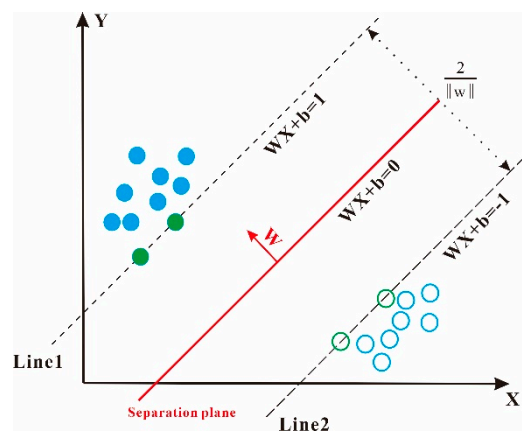


Figure 5. Support vector machine schematic.

A critical step in using non-linear SVMs is the selection of the kernel function, which performs a special spatial non-linear transformation, resulting in the projection of the training data into a high-dimensional feature space, which directly determines the dimensionality of the classification function. Ultimately, the optimal classification surface is found in the high-dimensional space, facilitating the classification calculations. SVM classification was carried out using ENVI 5.6; the radial basis kernel function (Gaussian radial function), which has high accuracy for classifying data, was chosen as the kernel function in this study, with the penalty parameter set to 100.

Owing to the narrowband and full spectral coverage of the SVC spectroradiometer, it is possible to effectively characterize the subtle spectral differences of rocks collected in the field. The measured feature spectral information is compared with the spectral information of remote sensing image elements to improve the accuracy and efficiency of training sample selection in remote sensing images. The measured spectra need to be resampled to the corresponding spectral resolution conditions of the remote sensing image when performing the comparison verification. The multivariate training element features are extracted using texture features, spectral index features, vegetation index features, and terrain features for different regions and levels of data limitation. The training samples obtained by the SVM method were all located within the field sampling work area and were analyzed by mineral rock identification. The rock samples collected covered four types of rocks: gabbro, Lujavrite, basalt, and Naujaite; Lujavrite, which is associated with the radioactive uranium ore, was analyzed by petrographic identification microscopy, and the collected samples all contained high mineral contents of eudialyte (Figure 6). Consequently, the SVM training samples were selected to create samples from these four lithologies, with a total of 653 samples (including 155 gabbro, 203 lujavrite, 105 basalt, and 190 naujaite).

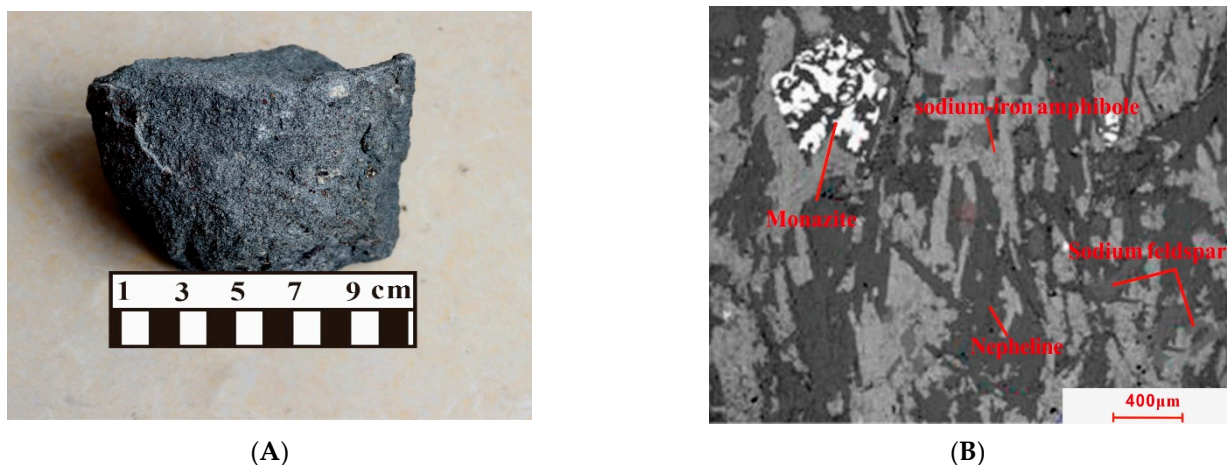


Figure 6. (A) Lujavrite hand specimen; (B) microscopic photograph of Lujavrite.

3.4. Thermal Anomaly Information Extraction

Hydrothermal-type uranium deposits lead to surface thermal anomalies when they are formed and also have some influence on the geothermal flow in their vicinity after formation. Therefore, points with a high distribution of surface thermal anomaly values tend to be spatially coherent with uranium ores. Geothermal signatures are also used by some researchers as an indicator of hydrothermal uranium deposits, which are often closely related to their distribution in deep uranium exploration [25,57]. Surface temperature inversion is closely related to various resource and environmental processes on the Earth's surface. As an important physical parameter of the energy balance and circulation interchange processes between the Earth and the air, understanding the surface temperature has become an important facet of the field of quantitative remote sensing. In this study, the radiative transfer equation (RTE) method, which is well established and widely applicable, is used to invert the surface temperature in the study area, which has a solid physical

basis due to its early development and high accuracy [58]. The RTE method is based on real-time atmospheric profile data, including humidity, temperature, and pressure, and uses radiant energy values obtained from individual thermal infrared bands observed by satellites—while removing atmosphere-related effects—to invert the surface temperature. RTE converts the thermal radiation values to surface temperatures after subtracting the influence of the atmospheric extinction coefficient as a parameter factor, whereby the atmospheric thermal radiation influence values can be obtained on the basis of atmospheric data (Table 2) [45,59]. The calculation is shown in Equation.

$$L_{\text{sensor}} = [\varepsilon B(T_s) + (1-\varepsilon)L_{\downarrow}] \tau + L_{\uparrow} \tag{1}$$

$$B(T_s) = [L_{\text{sensor}} - L_{\uparrow} - \tau(1-\varepsilon)L_{\downarrow}] / \tau\varepsilon \tag{2}$$

Table 2. Atmospheric profile parameters.

Data Type	Imaging Time	Atmospheric Transmissivity τ	Atmospheric Upward Radiation L_{\uparrow} (w/m ² /sr/ μ m)	Atmospheric Downward Radiance L_{\downarrow} (w/m ² /sr/ μ m)
Landsat TIRS10	7 August 2018	0.95	0.30	0.53
	29 July 2018	0.92	0.51	0.87
	26 August 2019	0.96	0.24	0.42

T_s is the surface temperature, in Kelvin; the blackbody radiance is denoted by B ; L denotes the radiance, where the arrows pointing up and down represent the upward and downward radiance of the atmosphere; and the surface-specific radiance and the atmospheric transmittance in the thermal infrared band are denoted by ε and τ , respectively. Due to the continuous atmospheric profile, the atmospheric parameters vary at different altitudes, which also results in differences in atmospheric radiance. The two core parameters in the RTE algorithm are the atmospheric upward and downward radiation and the atmospheric transmittance parameters, for which the surface temperature is calculated using the following formula:

$$T_s = K_2 / \ln(1 + K_1 / B(T_s)) \tag{3}$$

where K_2 and K_1 are constants that depend on the selected satellite metadata.

3.5. Remote Sensing Mineralization Prediction Based on the Weight of Evidence Methods

Agterberg proposed the Weight of Evidence Method (WofE), a geostatistical-based approach to mineralization prediction, using a Bayesian statistical analysis model [60]. The method aims to extract favorable areas (prospective areas) for mineralization, using geological information related to the formation of mineralization, overlaying and fusing such information, and analyzing it, which fully integrates AI technology, image analysis technology, and mathematical statistics technology. This approach is achieved by splitting all evidence layers into binary variables; in other words, evidence layers containing only '0' and '1' attributes, where '0' means that a single unit of evidence in the element layer does not exist (no ore), and '1' means that it does (contains ore). Assuming the number of units in the study area is expressed as S , the event element A is expressed as an element layer (hydrothermal alteration anomaly, mineral control structure, SVM classified lithology, radiothermal anomaly, etc.), and B is expressed as an ore-bearing unit. $P(B) = \text{Area}(B) / \text{Area}(S)$ denotes the prior probability of event B , where $\text{Area}()$ denotes the area. Bayesian statistical relations were introduced in the study area as the basis for the criterion, with A_i^+ , A_i^- denoting the presence and absence of A_i favorable conditions, respectively, which divided the study area into four pooled parts, expressed as $B^+ \cap A_i^+$, $B^+ \cap A_i^-$, $B^- \cap A_i^+$, $B^- \cap A_i^-$. The posterior probability is calculated using the following formula:

$$(B | A_1 A_2 \cdots A_n) = e^{\sum_{i=0}^n W_i} / 1 + e^{\sum_{i=0}^n W_i} \tag{4}$$

For each evidence layer, it is necessary to introduce a contrast value C , $C = W^+ - W^-$, in order to express its correlation with the deposit or occurrence. The strength of the correlation is indicated by a significant C value, with a positive or negative C value representing a positive or negative relationship between the layer and the indicative mineralization. Studentized Index (SI) defined as:

$$SI = C / \sqrt{\delta^2(W^+) + \delta^2(W^-)} \quad (5)$$

The evidence elements in the layers were verified against each other in groups of two, the weights of the evidence elements were calculated, and the layers were combined statistically using superposition analysis to obtain the final posterior probability distribution of mineralization.

4. Results and Analysis

4.1. Remote Sensing for Geological Background Information Extraction

A total of 13 lithologies have been interpreted, including gabbro, syenite, ditroite, and Lujavrite; Lujavrite—containing steenstrupine and eudialyte—is the main ore mineral in the study area (Figure 7). Based on the tectonic features of the Narsaq area, interpretation markers were established to obtain the distribution pattern of lineaments and rings in the area. Four faults, nine rings, and 157 tectonic joints were interpreted (Figure 7). The mean linear orientation of the interpreted linear structures was analyzed using ArcGIS linear analysis, which calculated that the mean linear orientation of the linear structures across the study area is 62° (azimuthal), i.e., the tectonics in the study area—as a whole—are predominantly NEE oriented (Figure 8A). The strike rose diagram shows that the highest frequency of tectonics is between the north–north-east and north-east–east orientations (Figure 8B), which is spatially consistent with the distribution of the Southern Rift Zone.

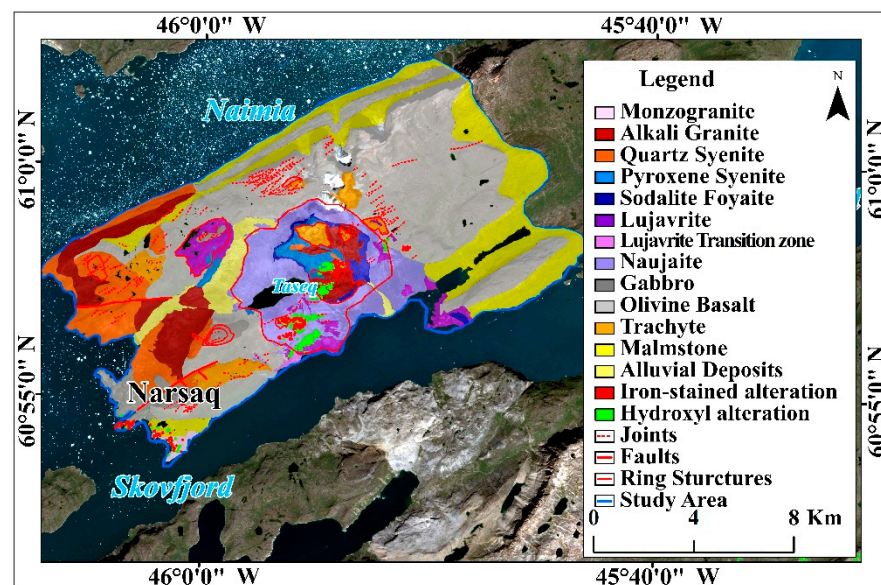


Figure 7. Interpreted map of remote sensing geological background information map (the base image is a combination of the 432 Sentinel-2 bands).

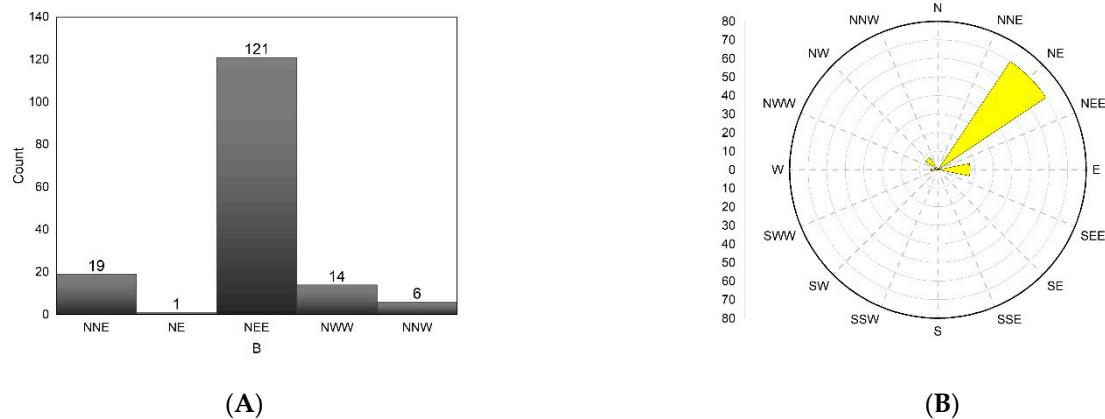


Figure 8. (A) Linear tectonic strike statistical histogram; (B) Linear tectonic strike rose diagram.

The hydroxy and iron-stained alteration is distributed in the center and lower parts of the study area, with the iron-stained alteration exhibiting a mass-like character and the hydroxy alteration showing a striped northeast spreading character. The two types of alteration information are mainly consistent with the location of surface outcrops of Naujaite and Lujavrite, which is indicative of the lithology.

4.2. Lithology Extraction Based on SVM

4.2.1. Lithological Information Enhancement and Analysis

Spectral absorption features were calculated using the IDL DISPEC software [1]. These features describe the shape of the spectrum, as reflected by the depth, width, area, and asymmetry (Table 3). The Lujavrite associated with the mineralization has the following characteristics (Figure 9): (i) a slowly rising plateau in the wavelength range of 1.0–1.3 μm ; (ii) an extremely strong absorption valley in the spectrum of 1.9–2.0 μm , which indicates that the Lujavrite exhibits absorption properties in the near-infrared band. (iii) The absorption spectrum after continuum removal has a maximum absorption valley depth of 47.87 at 0.4 μm —the area enclosed by the envelope and the spectral curve is the largest here, and the diagnostic spectrum is located at 0.4 μm . It also shows strong absorption characteristics at 1.92 μm and 1.42 μm , as reflected in Table 3, which proves that it is influenced by the vibration of water molecules and the leap of hydroxyl ions.

4.2.2. Feature Information Extraction

In SVM lithology extraction, two major dimensions—texture information and topographic information—were used. The texture information was calculated using PCA and the greyscale formula matrix. WV-2 image data were used, whose spectrum covers the range of 0.4–1.04 μm ; in this range, it is clear from the characteristic absorption in Table 3 that the Lujavrite has strong absorption properties in the coastal band and strong reflection properties in the near-infrared band. Further, the most informative bands of the image are concentrated in the true color band; therefore, bands one, two, five, and eight were selected for image enhancement using PCA (Figure 10B), and this image was used in the extraction of lithological PCA texture information. The texture information of WV-2 was also extracted using the greyscale formula matrix, and contrast (Figure 10C), angular-second-order moments (Figure 10D), homogeneity (Figure 10E), and phase dissimilarity (Figure 10F) were selected as feature statistics. The topographic relief was calculated using the slope information extracted from the DEM (Figure 10A). Before classification, the terrain and texture rasters were spatially resampled to ensure that the information had the same image size.

Table 3. Spectral absorption characteristics of lujavrite.

Wavelength (μ)	Depth	Wide	Area	Asymmetry
0.40	47.87	0.37	18.02	0.78
1.92	30.84	0.20	6.41	0.84
1.42	10.72	0.12	1.31	0.61
1.66	4.80	0.07	0.37	0.81
1.28	0.20	0.02	0.004	1

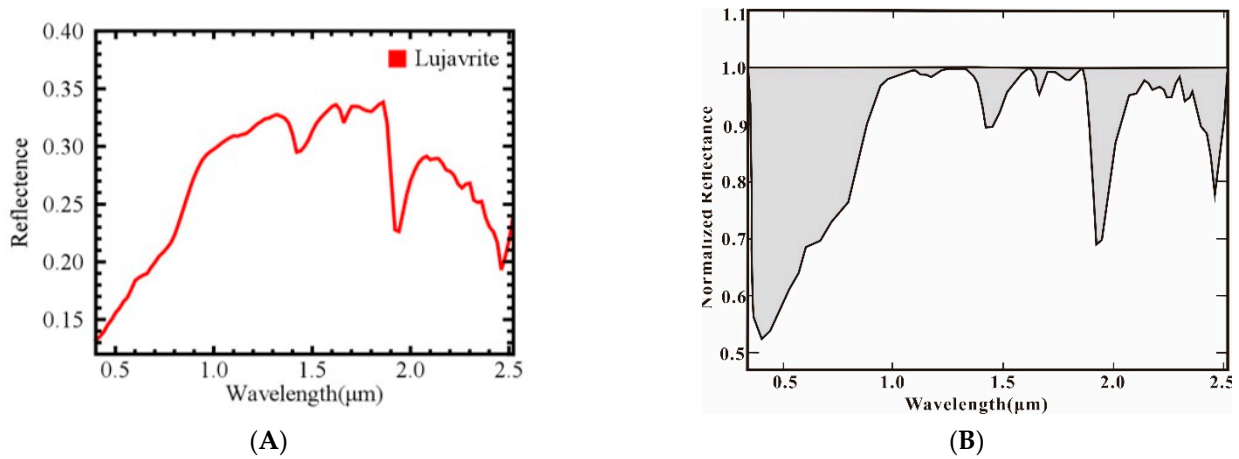


Figure 9. (A) Absorption characteristics of the continuum removal spectra of Lujavrite; (B) Characterization of the in situ spectra of Lujavrite.

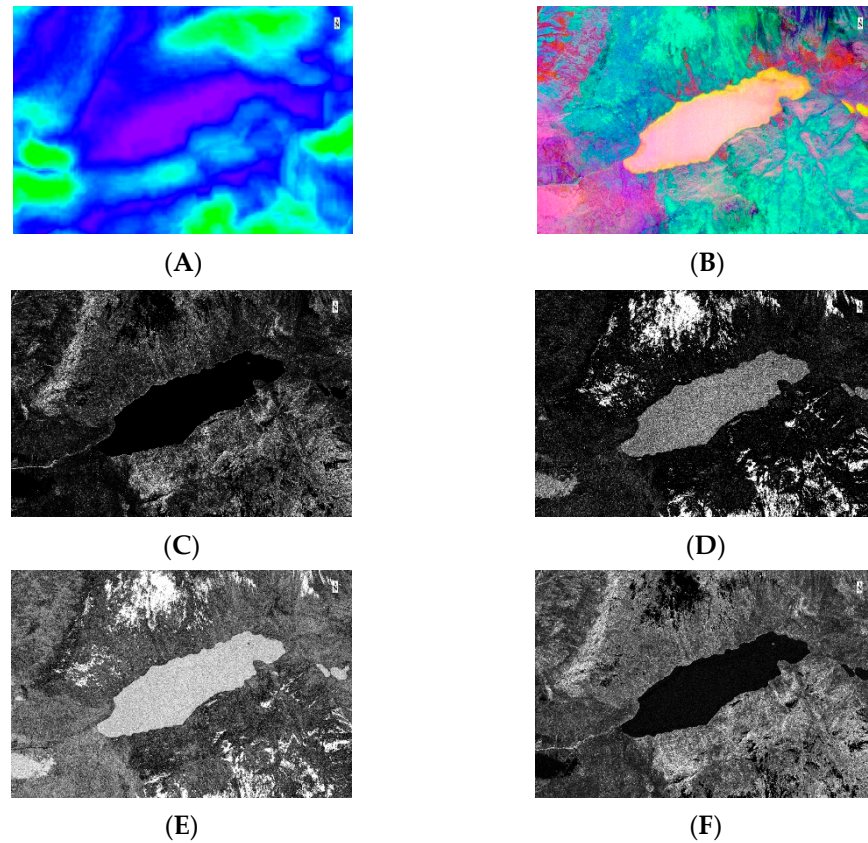


Figure 10. (A) Relief feature; (B) PCA feature; (C) Contrast feature; (D) Angular second-order moment feature; (E) Homogeneity feature; (F) Phase dissimilarity feature.

4.2.3. Results of SVM Lithology Classification

The classification images obtained by the SVM algorithm would show missing data in the classification patches, which were processed using majority/minority analysis to categorize the missing data into a category with a large percentage of surroundings; this helped eliminate the missing classification data. The geological map of the field survey and the remotely interpreted geological map of the area were used to compare and verify the classification results of the Lujavrite (Figure 7). From the classification results, patches with single texture and terrain information were significantly better classified than patches with complex information. In patches with complex feature classes and redundant terrain information, terrain features and texture features could not be accurately distinguished by the SVM algorithm. This is because high spatial resolution satellite data have a limited wavelength and low spectral resolution, making it difficult to distinguish between small diagnostic spectral information in the mixed image elements and reducing the accuracy of the algorithm’s recognition. Lujavrite orthoclase is mainly clustered in the central and northern part of the study area and is distributed in bands (Figure 11).

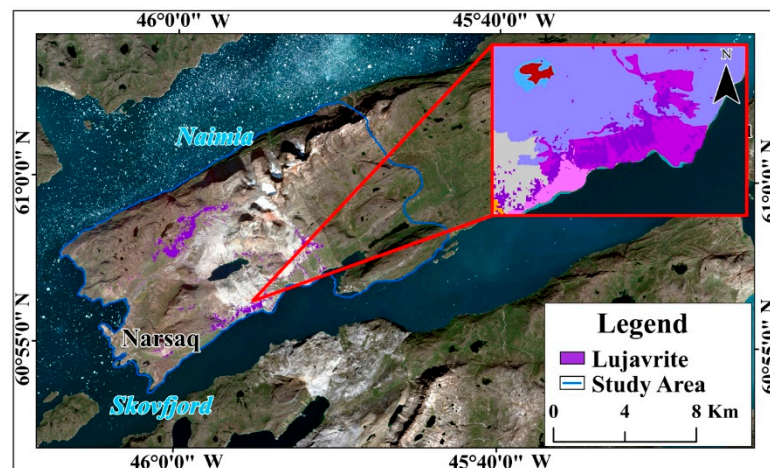


Figure 11. SVM Lithology classification map (the base image is a combination of Worldview-2/s 321 bands).

The accuracy of the SVM lithology classification results was evaluated, as shown in Table 4. It is clear from the table that the classification user accuracy of the main mineralized lithology, namely the Lujavrite, is 89.57%; the overall accuracy of SVM classification is 87.75%, with a kappa coefficient of 0.84. After field route verification, dense grey Lujavrite was seen in the target route (Figure 12C), and the rocks were lined with oriented sodium–iron amphibole with a banded structure (Figure 12B), which is consistent with the region shown in the circle.

Table 4. Result accuracy evaluation table for classification using SVM.

Lithological Category	Lithological Category (Ground Truth Data)					User Accuracy
	Gabbro	Lujavrite	Basalt	Naujaite	Total	
Gabbro	134	4	9	8	155	86.45%
Lujavrite	4	189	1	17	211	89.57%
Basalt	13	0	94	9	116	81.03%
Naujaite	4	10	1	156	171	91.23%
Total	155	203	105	190	653	
Producer accuracy	86.45%	93.10%	89.52%	82.11%		

Overall Accuracy = 87.75%; Kappa coefficient = 0.84.

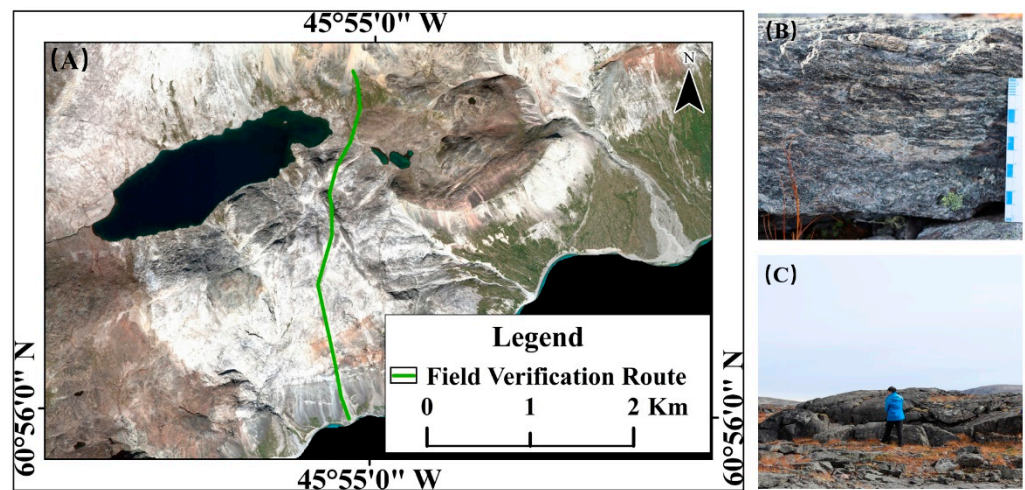


Figure 12. (A) Field validation route map (the base image is a combination of Sentinel-2's 432 bands); (B,C) Greyish-black dense Lujavrite.

4.3. Thermal Anomalies Extraction of Radioactive Minerals

Most of the uranium equivalents in the study area are greater than 4.3×10^{-6} , while the distribution pattern of greater than 5.2×10^{-6} is more consistent with the distribution pattern of nepheline syenite, proving that nepheline syenite is highly radioactive [61]. The arfvedsonite Lujavrite associated with rare earth-uranium mineralization is rich in elements such as U and Th, which are highly radioactive. The regional sandstone zone is composed mainly of feldspathic quartzite and contains radioactive minerals that have been subjected to low-pressure-high-temperature metamorphism and, thus, exhibit thermal anomalies in surface temperature. Over a given year, the average temperature in the study area is below 0°C ; the surface temperature is extremely low in winter due to the snow and ice cover, whereas water bodies are somewhat insulated, which leads to a lower surface temperature than the water body temperature. This masks the trace thermal anomalies of radioactive elements. The summer images were selected for use because there is less snow and ice cover during this season; further, the difference between the surface temperature of water bodies and land is significant, and the land surface temperature is greater than 0°C . With Landsat's thermal infrared band, it is possible to effectively distinguish surface temperature differences and, thus, determine areas with radiothermal anomalies.

The Landsat TIRS 10 band was utilized for the surface temperature inversion using the RTE method. Thermal anomalies in the study area were mainly concentrated in the south-central part of the study area, where the overall surface temperature was low, and the average surface temperature in summer ranged from 5° to 16° , with the highest surface temperature values reaching 28° in some areas. Among them, there are three typical high-temperature areas (Figure 13): L1, L2, and L3 (Table 5). All three thermal anomalies are located in the vicinity of the southern rift zone, and the lithology of the high-temperature area is mainly alkaline rock body Naujaite and arfvedsonite Lujavrite; the arfvedsonite type ore is accompanied by uranium, thorium, and other elements, with obvious radioactive anomalies. The thermal anomalies exhibited a strong correlation with both faults and lithology in the area, which further suggests that surface temperature anomalies are indicative of mineralization. In conclusion, the thermal anomalies in the study area could mainly be found along the upper part of the Ilimaussaq Complex on the land margin, and the exposed lithology was arfvedsonite Lujavrite, exhibiting a blocky distribution of NE spreading. In some linear tectonically dense areas, the surface temperature values were significantly higher than those in the surrounding area, indicating that the surface temperature has some correlation with the tectonics. The distribution of thermal anomalies is somewhat indicative of the lithology, linear tectonics, and mineral distribution.

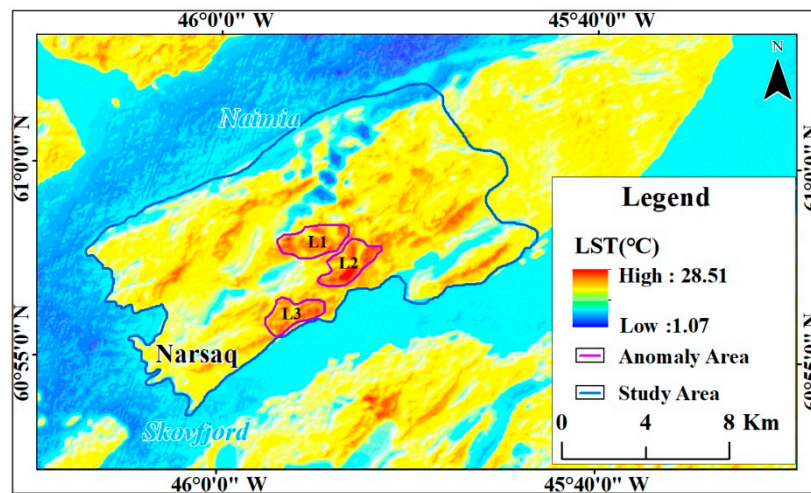


Figure 13. Surface temperature inversion map.

Table 5. Surface temperatures in areas of thermal anomalies.

Abnormal Area	Maximum Surface Temperature	Minimum Surface Temperature	Average Surface Temperature
L1	28.51	15.70	23.85
L2	27.08	14.59	22.76
L3	26.32	16.64	23.24
Study area	28.51	1.07	16.85

Through the official websites of the Geological Survey of Denmark and Greenland (De Nationale Geologiske Undersøgelser for Danmark og Grønland, GEUS), certain airborne radiometric data were selected for the Narsaq area: total uranium gamma radiation, uranium concentration (ppm), and thorium concentration (ppm) (Figure 14). These data were obtained from the GEUS South Greenland Regional Uranium Exploration Project (SYDURAN) [62], which used a helicopter-borne Scintrex GAD-6 for radiometric measurements. The correlation between this airborne radiation data and surface temperature inversion data was analyzed using the Spearman’s correlation coefficient, and the thermal anomalies were found (Table 6) to be positively correlated with the total uranium gamma radiation, uranium, and thorium elements, with correlation coefficients of 0.63, 0.60, and 0.65, respectively. This further indicates that the surface temperature thermal anomalies are indicative of the presence of radioactive elements.

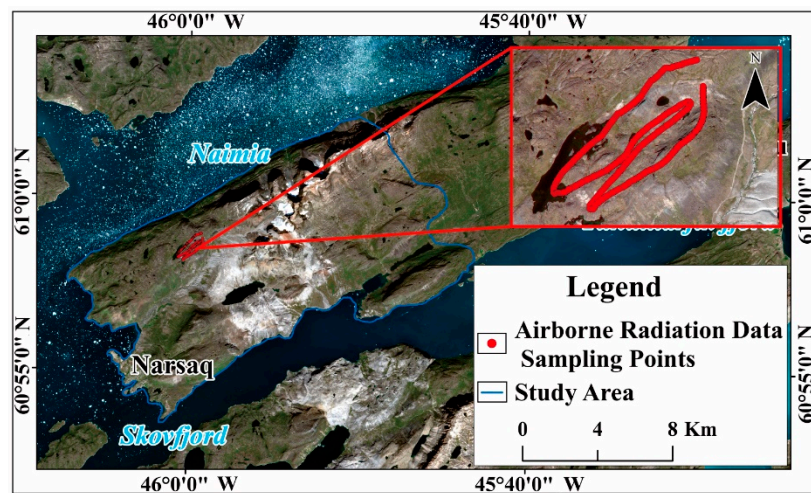


Figure 14. Map of sampling points for airborne radiation data.

Table 6. Correlations between thermal anomalies and radioactive elements.

Types	Spearman's Correlation Coefficient
Total uranium gamma radiation	0.63
U ppm	0.60
Th ppm	0.65

4.4. Mineral Prospectivity Mapping Based on Remote Sensing and Weight-of-Evidence Model

Mineralization is controlled by the formation lithology of a certain era, either directly or indirectly. Ore-bearing rock masses usually are more easily outcropped than the ore body, making the outcropping area larger. Ore-bearing rock masses closely related to the ore body are the marker bed for prospecting. The ore body can be delineated by tracking the ore-bearing rock masses [63]. Mineralization in the study area is mainly associated with Lujavrite, where black, dense, fine-grained arfvedsonite Lujavrite forms arfvedsonite ores, and mineralization elements such as rare earth elements and uranium are hosted in paragenetic minerals formed by the cooling and crystallization of magma. Research has shown that the mineralized minerals include steenstrupine, selenopatite, cerium phosphate sodalite, monazite, zirconium silicate minerals, etc. There are 13 types of mineralized minerals, among which the most important rare earth minerals are steenstrupine (5.58%), followed by monazite (0.09%), and sodium phosphorite, which are often found in agglomerates and contain associated uranium, thorium, and other elements; in regions where these are found, radioactive anomalies are very obvious [40,64–67]. By identifying such radioactive Lujavrite via remote sensing, the mineralization target area can be effectively traced. The main ore finding signatures in the study area are as follows: (1) Lithological and tectonic signatures—uranium-bearing minerals are concentrated in Lujavrite, among which the arfvedsonite type is the most important. The mineralization process is easily controlled by regional north-east tectonics, and tectonic activity often leads to strong deformations in the mineralized area, with the tectonic and hydrothermal alteration information output locations spreading north-eastwards, in parallel. (2) Thermal anomaly signatures—uranium ore is a radioactive mineral, and areas of radioactive thermal anomalies can be extracted in low-temperature areas using surface temperature thermal anomalies.

The study area was decomposed into 67,243 analysis units according to 10 m pixel units. The multi-layer raster data were imported for calculation using the ArcGIS geographic information analysis software developed by Esri.on. Through a comprehensive analysis of the aforementioned signatures, the four main elements of the weight of evidence were selected to include SVM machine learning lithological classification information, tectonic information, PCA hydrothermal alteration information, and surface thermal anomaly information. The comprehensive evaluation values corresponding to the four evidence elements were calculated through a priori probability analysis brought into the weight-of-evidence method (Table 7). A final probability map of favorable areas of mineralization in the study area was generated, with areas of high favorability values being spatially consistent with known mineralization in the study area (Figure 15).

Table 7. Statistical parameters for the binarization of evidence layers.

Evaluation Index Layer	W^+	$\sigma(W^+)$	W^-	$\sigma(W^-)$	C	SI	W
Thermal anomalies	4.44	1.05	−0.82	0.38	5.26	4.69	4.44
SVM	4.33	1.06	−0.68	0.36	5.01	4.47	4.33
Hydrothermal alteration	3.35	1.15	−0.20	0.28	3.55	2.98	3.35
Structural density	0.59	0.30	−1.07	0.58	1.67	2.52	0.59

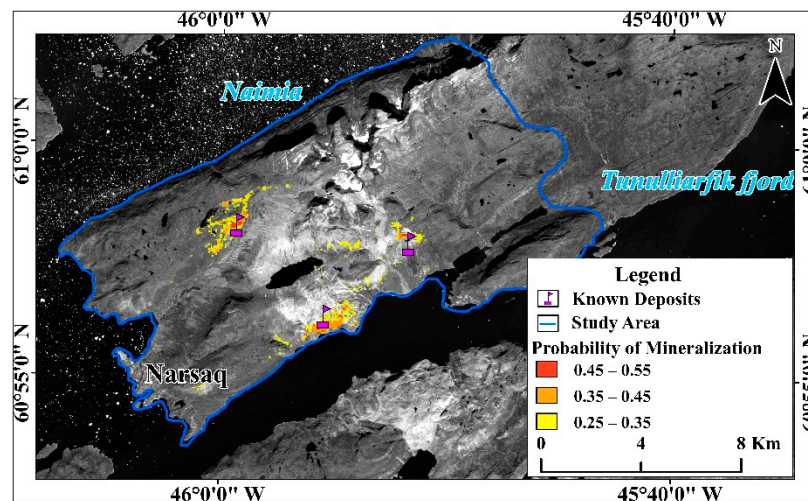


Figure 15. Map of projected potential mineralization areas (the base image was made using the Sentinel-2 panchromatic band).

The high probability area in the mineralization prediction map mainly covers the lithologies of Lujavrite and Naujaite. Combined with geological materials and field investigations, the uranium-bearing minerals are concentrated in the Lujavrite, with the arfvedsonite type being the most abundant. The mineralization is susceptible to regional north-east tectonic control, and tectonic activity often leads to the strong deformation of the mineralized area, with a parallel north-east spreading of tectonic and hydrothermal alteration information output locations. The alteration is dominated by alkaline alteration, enriching radioactive minerals in low-temperature areas; using surface temperature thermal anomalies can extract areas of radioactive thermal anomalies, and the average value of temperature anomalies in the predicted area is 23.24 °C (Figure 16).

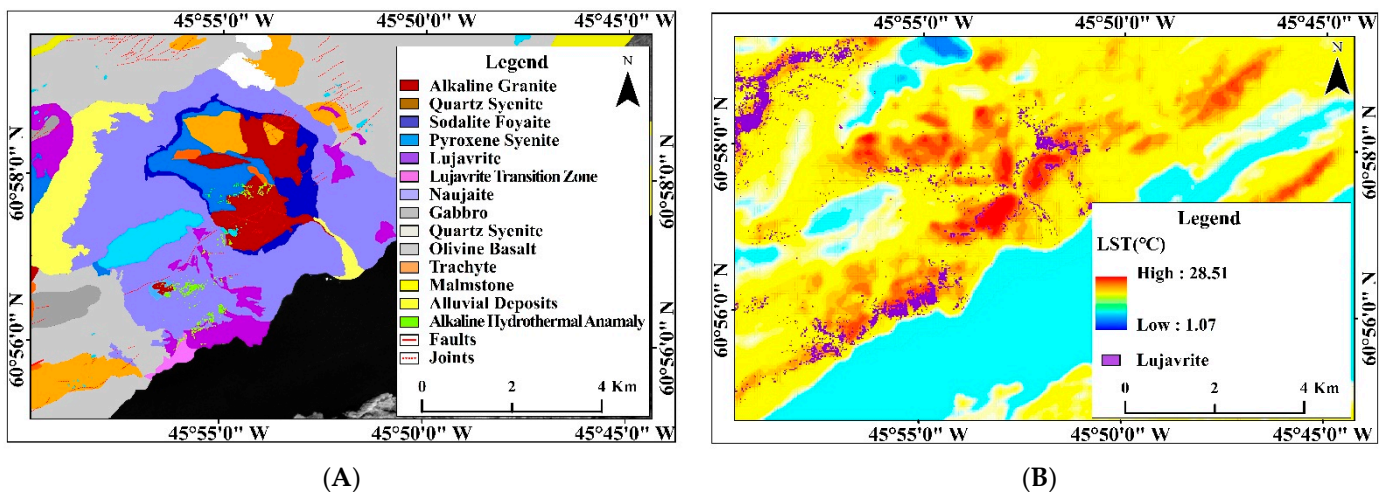


Figure 16. (A,B) Mineral prospecting target area analysis map.

5. Discussions

High latitudes are heavily ice-covered, making it difficult for remote sensing to detect surface anomalies, with snow up to tens of meters thick completely covering any remote sensing information. However, in some areas, the snow and ice cover varies seasonally, as is the case in the southern Greenland region. The most significant advantage of remote sensing imagery is the multiplicity of data and the long time-series features, which facilitates the detection of geological phenomena irrespective of season or temperature. The use of remote sensing to detect geothermal heat is relatively diverse but is mainly carried out by detecting surface heat sources, such as volcanoes and hot springs [29,31,68,69]. The use

of surface temperature inversion results to identify areas of high-temperature anomalies for the purpose of mapping the distribution of radioactive element enrichment zones is a novel method for undertaking geological mineralization surveys. In the harsh temperatures of the Narsaq region of Greenland, even small thermal anomalies can be captured by the thermal infrared sensor, which can be useful for identifying radioactive element enrichment zones in high latitudes. All types of data, including ASTER data, Sentinel Data-3, and Landsat TIRS data, there are limitations in terms of the resolution of the extracted surface temperature products, and there is a bias in the identification of specific geographical features [58,59,70,71]. With the SVM extraction method that used the in situ spectrum as a reference, the variation in the shape of the spectrum curve of the image elements within a rock unit, the variation in the position of the absorption valley, and the reflection peak (spectral difference), and the sample separability between the rock units affect the accuracy of the SVM classification. However, the SVM method was combined with the thermal anomaly inversion method to extract arfvedsonite Lujavrite-containing radioactive minerals in the region, and the two methods were used to corroborate the accuracy of the results. Further, Crosta's hydrothermal alteration information extraction technique [36,72,73] was utilized to extract relevant alteration information in the alkaline rock area, and the interpreted mineral control tectonic spreading characteristics were applied to the Lujavrite outcrop such that the mineralization characteristics could be optimized. This overlay analysis of multiple remote sensing data can increase the prediction accuracy while also solving the issue of predicting mineralization in areas of weak information. The geophysical and geochemical data in most areas of mineralization prediction are small-scale and do not have raster digitization. For small-range or large-scale mineralization studies, the accuracy of such data is severely lacking and, therefore, does not accurately reflect the geological and geochemical information of the area. The importance of such elements could not be measured while using this mineralization methodology. Such elements need to be refined in future studies by complementing them with large-scale studies. As the types of mineralization are not abundant in this article, it is not possible to build a sound statistical model, and more areas need to be studied. Although the use of remote sensing alone to support mineralization prediction is efficient and comprehensive, quantitative mathematical methods with multiple types of parameters should be used, and there is a need to add more geological anomaly information evaluation indicators to the research method to develop a more comprehensive method for mineralization prediction at larger scales.

6. Conclusions

A highly efficient and novel technical tool for regional mineralization investigations is proposed, which uses the remote sensing inversion of radiothermal anomalies in high-latitude areas. The study area is rich in radioactive minerals, and the average year-round temperature is below 0 °C, allowing weak thermal radiation to manifest through surface temperature anomalies. Landsat 8 thermal infrared data were used to invert the surface temperature using the RTE model to circle the high thermal anomaly area. The average surface temperature of the high thermal area was 23.28 °C, which was higher than the average temperature of the entire area, of 16.85 °C. By conducting Spearman correlation analyses with the airborne radiation data, a positive correlation with the uranium and thorium concentration and the correlation coefficients all exceeded 0.6, indicating that the thermal anomaly remote sensing inversion technique is a good indicator of low-temperature radioactive mineral enrichment areas. By establishing texture and topographic features, the SVM algorithm was used to identify the mineralized lithology of Lujavrite, with a classification accuracy of 89.57%; the classification results revealed that the Lujavrite was characterized by banded outcrops. Through the comprehensive analysis of remote sensing information, combined with metallogenic background information, the study area was deemed to be a favorable area for mineralization through the weight-of-evidence model, with high-value areas of mineralization potential overlapping well with known mineralization areas. The combination of remote sensing thermal anomaly information

and rock interpretation methods in the Narsaq region of Greenland has, therefore, been validated for the analysis of mineralization in the region, and this integrated approach to remote sensing information can be extended to the prediction of mineralization in radiogenic high-altitude areas.

Author Contributions: Conceptualization, P.L., L.H. and Z.H.; methodology, P.L., L.H. and Z.H.; software, P.L.; validation, P.L., L.H. and Z.H.; formal analysis, P.L.; investigation, P.L., J.Z., B.H., Y.Y. and L.X.; resources, Z.H., J.Z. and B.H.; data curation, P.L., H.H. and Y.Z.; writing—original draft preparation, P.L., H.H. and Y.Z.; writing—review and editing, P.L., L.H. and Z.H.; visualization, P.L., L.H. and Z.H.; supervision, L.H. and Z.H.; project administration, Z.H. and J.Z. All authors have read and agreed to the published version of the manuscript.

Funding: This research received no external funding.

Data Availability Statement: Not applicable.

Acknowledgments: The authors would like to thank the following educational and research institutions for the infrastructure: Chengdu University of Technology (CDUT), Institute of Multipurpose Utilization of Mineral Resources, China Geological Survey. Without the support of these institutions this study could not be performed.

Conflicts of Interest: No potential conflict of interest was reported by the authors. The authors declare that they have no known competing financial interests or personal relationships that could have appeared to influence the work reported in this paper.

References

1. Hecker, C.; van Ruitenbeek, F.J.A.; van der Werff, H.M.A.; Bakker, W.H.; Hewson, R.D.; van der Meer, F.D. Spectral Absorption Feature Analysis for Finding Ore A tutorial on using the method in geological remote sensing. *IEEE Geosci. Remote Sens. Mag.* **2019**, *7*, 51–71. [[CrossRef](#)]
2. Hunt, G. Spectral Signatures of Particulate Minerals in the Visible and Near Infrared. *Geophysics* **1977**, *42*, 501–513. [[CrossRef](#)]
3. Clark, R.N.; King, T.V.V.; Klejwa, M.; Swayze, G.A.; Vergo, N. High spectral resolution reflectance spectroscopy of minerals. *Int. J. Rock Mech. Min. Sci. Geomech. Abstr.* **1991**, *28*, A217. [[CrossRef](#)]
4. Bierwirth, P.; Huston, D.; Blewett, R. Hyperspectral mapping of mineral assemblages associated with gold mineralization in the Central Pilbara, Western Australia. *Econ. Geol. Bull. Soc. Econ. Geol.* **2002**, *97*, 819–826. [[CrossRef](#)]
5. Kruse, F.A.; Perry, S.L.; Caballero, A. District-level mineral survey using airborne hyperspectral data, Los Menucos, Argentina. *Ann. Geophys.* **2006**, *49*, 83–92.
6. Rockwell, B.W.; Cunningham, C.G.; Breit, G.N.; Rye, R.O. Spectroscopic mapping of the White Horse alunite deposit, Marysvale Volcanic Field, Utah: Evidence of a magmatic component. *Econ. Geol.* **2006**, *101*, 1377–1395. [[CrossRef](#)]
7. Abulghasem, Y.A.; Akhir, J.B.M.; Hassan, W.F.W.; Samsudin, A.; Youshah, B.M. The use of remote sensing technology in geological investigation and mineral detection in Wadi shati, Libya. *Electron. J. Geotech. Eng.* **2012**, *17*, 1279–1291.
8. Amer, R.; Kusky, T.; Ghulam, A. Lithological mapping in the Central Eastern Desert of Egypt using ASTER data. *J. Afr. Earth Sci.* **2010**, *56*, 75–82. [[CrossRef](#)]
9. Xu, Y.; Chen, J.; Meng, P. Detection of alteration zones using hyperspectral remote sensing data from Dapingliang skarn copper deposit and its surrounding area, Shanshan County, Xinjiang Uygur autonomous region, China. *J. Vis. Commun. Image Represent.* **2019**, *58*, 67–78. [[CrossRef](#)]
10. Milovsky, G.A.; Makarov, V.P.; Troitsky, V.V.; Lyamin, S.M.; Orlyankin, V.N.; Shemyakina, E.M.; Gil, I.G. Use of Remote Sensing to Find a Localization Pattern of Gold Mineralization in the Central Part of the Ayan-Yuryakh Anticlinorium, Magadan Oblast. *Izv. Atmos. Ocean. Phys.* **2019**, *55*, 1389–1394. [[CrossRef](#)]
11. Yamaguchi, Y.; Kahle, A.B.; Tsu, H.; Kawakami, T.; Pniel, M. Overview of advanced spaceborne thermal emission and reflection radiometer (ASTER). *IEEE Trans. Geosci. Remote Sens.* **1998**, *36*, 1062–1071. [[CrossRef](#)]
12. Dehnavi, A.G.; Sarikhani, R.; Nagaraju, D. Image Processing and Analysis of Mapping Alteration Zones in environmental research, East of Kurdistan, Iran. *World Appl. Sci. J.* **2010**, *11*, 278–283.
13. Gupta, P.; Venkatesan, M. *Mineral Identification Using Unsupervised Classification from Hyperspectral Data*; Springer: Singapore, 2020.
14. Shayeganpour, S.; Tangestani, M.H.; Gorsevski, P.V. Machine learning and multi-sensor data fusion for mapping lithology: A case study of Kowli-kosh area, SW Iran. *Adv. Space Res.* **2021**, *68*, 3992–4015. [[CrossRef](#)]
15. Liu, Z.; Cao, J.; You, J.; Chen, S.; Lu, Y.; Zhou, P. A lithological sequence classification method with well log via SVM-assisted bi-directional GRU-CRF neural network. *J. Pet. Sci. Eng.* **2021**, *205*, 108913. [[CrossRef](#)]
16. Gu, Y.; Zhang, D.; Bao, Z.; Guo, H.; Zhou, L.; Ren, J. Lithology prediction of tight sandstone formation using GS-LightGBM hybrid machine learning model. *Bull. Geol. Sci. Technol.* **2021**, *40*, 224–234.

17. Mou, D.; Zhang, L.; Xu, C. Comparison of Three Classical Machine Learning Algorithms for Lithology Identification of Volcanic Rocks Using Well Logging Data. *J. Jilin Univ. Earth Sci. Ed.* **2021**, *51*, 951–956.
18. Kumar, C.; Chatterjee, S.; Oommen, T.; Guha, A. Automated lithological mapping by integrating spectral enhancement techniques and machine learning algorithms using AVIRIS-NG hyperspectral data in Gold-bearing granite-greenstone rocks in Hutti, India. *Int. J. Appl. Earth Obs. Geoinf.* **2020**, *86*, 15. [[CrossRef](#)]
19. Duan, Y.; Zhao, Y.; Ma, C.; Jiang, W. Lithology Identification Method Based on Multi-layer Ensemble Learning. *J. Data Acquis. Process.* **2020**, *35*, 572–581.
20. Han, Q.; Zhang, X.; Shen, W. Application of Support Vector Machine Based on Decision Tree Feature Extraction in Lithology Classification. *J. Jilin Univ. Earth Sci. Ed.* **2019**, *49*, 611–620.
21. Hutchison, W.; Finch, A.A.; Borst, A.M.; Marks, M.A.W.; Upton, B.G.J.; Zerkle, A.L.; Stueken, E.E.; Boyce, A.J. Mantle sources and magma evolution in Europe’s largest rare earth element belt (Gardar Province, SW Greenland): New insights from sulfur isotopes. *Earth Planet. Sci. Lett.* **2021**, *568*, 117034. [[CrossRef](#)]
22. Steenfelt, A.; Kolb, J.; Thrane, K. Metallogeny of South Greenland: A review of geological evolution, mineral occurrences and geochemical exploration data. *Ore Geol. Rev.* **2016**, *77*, 194–245. [[CrossRef](#)]
23. Aydar, E.; Diker, C. Carcinogen soil radon enrichment in a geothermal area: Case of Guzelcamli-Davutlar district of Aydin city, western Turkey. *Ecotoxicol. Environ. Saf.* **2021**, *208*, 111466. [[CrossRef](#)] [[PubMed](#)]
24. Cui, Y.; Zhu, C.; Qiu, N.; Tang, B.; Guo, S. Radioactive Heat Production and Terrestrial Heat Flow in the Xiong’an Area, North China. *Energies* **2019**, *12*, 4608. [[CrossRef](#)]
25. Li, Q. *The Study of Deep Geothermal Features in Sichuan Basin*; Chengdu University of Technology: Chengdu, China, 1992.
26. Qing-yang, L.I.; Hui-rong, C.A.I.; Yan, C. The study and application of the relationship between the geothermal field and the deep uranium ore deposit. *Geol. China* **2010**, *37*, 198–203.
27. Wang, J.-h.; Zhang, J.-l.; Liu, D.-C. Discussion on the application potential of thermal infrared remote sensing technology in uranium deposits exploration. *World Nucl. Geosci.* **2011**, *28*, 32–41.
28. Salawu, N.B.; Fatoba, J.O.; Adebisi, L.S.; Eluwole, A.B.; Olasunkanmi, N.K.; Orosun, M.M.; Dada, S.S. Structural geometry of Ikogosi warm spring, southwestern Nigeria: Evidence from aeromagnetic and remote sensing interpretation. *Geomech. Geophys. Geo-Energy Geo-Resour.* **2021**, *7*, 26. [[CrossRef](#)]
29. Gemitzi, A.; Dalampakis, P.; Falalakis, G. Detecting geothermal anomalies using Landsat 8 thermal infrared remotely sensed data. *Int. J. Appl. Earth Obs. Geoinf.* **2021**, *96*, 102283. [[CrossRef](#)]
30. Rodriguez-Gomez, C.; Kereszturi, G.; Reeves, R.; Rae, A.; Pullanagari, R.; Jeyakumar, P.; Procter, J. Lithological mapping of Waitapu Geothermal Field (New Zealand) using hyperspectral and thermal remote sensing and ground exploration techniques. *Geothermics* **2021**, *96*, 102195. [[CrossRef](#)]
31. Xin, L.; Liu, X.; Zhang, B. Land surface temperature retrieval and geothermal resources prediction by remote sensing image: A case study in the Shijiazhuang area, Hebei province. *J. Geomech.* **2021**, *27*, 40–51.
32. Saibi, H.; Mia, M.B.; Bierre, M.; El Kamali, M. Application of remote sensing techniques to geothermal exploration at geothermal fields in the United Arab Emirates. *Arab. J. Geosci.* **2021**, *14*, 1251. [[CrossRef](#)]
33. Goldstein, B.A.; Hill, A.J.; Long, A.; Budd, A.R.; Holgate, F.; Malavazos, M. Hot dry rock geothermal exploration in Australia. *ASEG Ext. Abstr.* **2004**, *2004*, 1–4.
34. Wyborn, D.; Somerville, M. Prospective hot-dry-rock geothermal energy in Australia. GA Publication Research Newsletter. 1994. Available online: https://d28rz98at9flks.cloudfront.net/90424/ResearchNews_21_p001.pdf (accessed on 25 May 2022).
35. Coolbaugh, M.F.; Kratt, C.; Fallacaro, A.; Calvin, W.M.; Tarani, J.V. Detection of geothermal anomalies using Advanced Spaceborne Thermal Emission and Reflection Radiometer (ASTER) thermal infrared images at Bradys Hot Springs, Nevada, USA. *Remote Sens. Environ.* **2007**, *106*, 350–359. [[CrossRef](#)]
36. Aita, S.K.; Omar, A.E. Exploration of uranium and mineral deposits using remote sensing data and GIS applications, Serbal area, Southwestern Sinai, Egypt. *Arab. J. Geosci.* **2021**, *14*, 2214. [[CrossRef](#)]
37. Yousefi, M.; Tabatabaei, S.H.; Rikhtehgaran, R.; Pour, A.B.; Pradhan, B. Application of Dirichlet Process and Support Vector Machine Techniques for Mapping Alteration Zones Associated with Porphyry Copper Deposit Using ASTER Remote Sensing Imagery. *Minerals* **2021**, *11*, 1235. [[CrossRef](#)]
38. Marks, M.A.W.; Hettmann, K.; Schilling, J.; Frost, B.R.; Markl, G. The Mineralogical Diversity of Alkaline Igneous Rocks: Critical Factors for the Transition from Miaskitic to Agpaitic Phase Assemblages. *J. Petrol.* **2011**, *52*, 439–455. [[CrossRef](#)]
39. Steenfelt, A. High-technology metals in alkaline and carbonatitic rocks in greenland—Recognition and exploration. *J. Geochem. Explor.* **1991**, *40*, 263–279. [[CrossRef](#)]
40. Zhao, Y.; Lu, W.; Wang, A.; Lu, W. Research Progress on the Ilimaussaq Nb-Ta-U-REE Deposit, Greenland. *Geol. Sci. Technol. Inf.* **2013**, *32*, 9–17.
41. van der Werff, H.; van der Meer, F. Sentinel-2A MSI and Landsat 8 OLI Provide Data Continuity for Geological Remote Sensing. *Remote Sens.* **2016**, *8*, 883. [[CrossRef](#)]
42. Drusch, M.; Del Bello, U.; Carlier, S.; Colin, O.; Fernandez, V.; Gascon, F.; Hoersch, B.; Isola, C.; Laberinti, P.; Martimort, P.; et al. Sentinel-2: ESA’s Optical High-Resolution Mission for GMES Operational Services. *Remote Sens. Environ.* **2012**, *120*, 25–36. [[CrossRef](#)]

43. Updike, T.; Comp, C. Radiometric use of WorldView-2 imagery. DigitalGlobe. 2010, p. 1. Available online: <https://www.yumpu.com/en/document/read/43552535/radiometric-use-of-worldview-2-imagery-technical-note-pancroma> (accessed on 25 May 2022).
44. Irons, J.R.; Dwyer, J.L.; Barsi, J.A. The next Landsat satellite: The Landsat Data Continuity Mission. *Remote Sens. Environ.* **2012**, *122*, 11–21. [[CrossRef](#)]
45. Jimenez-Munoz, J.C.; Sobrino, J.A.; Skokovic, D.; Mattar, C.; Cristobal, J. Land Surface Temperature Retrieval Methods From Landsat-8 Thermal Infrared Sensor Data. *IEEE Geosci. Remote Sens. Lett.* **2014**, *11*, 1840–1843. [[CrossRef](#)]
46. Abrams, M.; Crippen, R.; Fujisada, H. ASTER Global Digital Elevation Model (GDEM) and ASTER Global Water Body Dataset (ASTWBD). *Remote Sens.* **2020**, *12*, 1156. [[CrossRef](#)]
47. Jing, C.; Bokun, Y.; Runsheng, W.; Feng, T.; Yingjun, Z.; Dechang, L.; Suming, Y.; Wei, S. Regional-scale mineral mapping using ASTER VNIR/SWIR data and validation of reflectance and mineral map products using airborne hyperspectral CASI/SASI data. *Int. J. Appl. Earth Obs. Geoinf.* **2014**, *33*, 127–141. [[CrossRef](#)]
48. Pour, A.B.; Hashim, M. The application of ASTER remote sensing data to porphyry copper and epithermal gold deposits. *Ore Geol. Rev.* **2012**, *44*, 1–9. [[CrossRef](#)]
49. Brown, M.; Lewis, H.G.; Gunn, S.R. Linear spectral mixture models and support vector machines for remote sensing. *IEEE Trans. Geosci. Remote Sens.* **2000**, *38*, 2346–2360. [[CrossRef](#)]
50. Brown, M.; Gunn, S.R.; Lewis, H.G. Support vector machines for optimal classification and spectral unmixing. *Ecol. Model.* **1999**, *120*, 167–179. [[CrossRef](#)]
51. Brown, M.; Lewis, H. Support vector machines and linear spectral unmixing for remote sensing. In Proceedings of the International Conference on Advances in Pattern Recognition (ICAPR 98), Plymouth, UK, 23–25 November 1998; pp. 395–404.
52. Lackner, M.; Conway, T.M. Determining land-use information from land cover through an object-oriented classification of IKONOS imagery. *Can. J. Remote Sens.* **2008**, *34*, 77–92. [[CrossRef](#)]
53. Tsang, I.W.; Kwok, J.T.; Cheung, P.M. Core vector machines: Fast SVM training on very large data sets. *J. Mach. Learn. Res.* **2005**, *6*, 363–392.
54. Xiao, A.; Zhao, W.; Hu, D.; Liu, L.; Li, J. Remote sensing information extraction based on object-oriented and support vector machines. *Sci. Surv. Mapp.* **2010**, *35*, 154–157.
55. Pasolli, E.; Melgani, F.; Tuia, D.; Pacifici, F.; Emery, W.J. SVM Active Learning Approach for Image Classification Using Spatial Information. *IEEE Trans. Geosci. Remote Sens.* **2014**, *52*, 2217–2233. [[CrossRef](#)]
56. Cortes, C.; Vapnik, V. Support-vector networks. *Mach. Learn.* **1995**, *20*, 273–297. [[CrossRef](#)]
57. Room, C.A.o.S.G. *Introduction to Mine Geothermal*; China Coal Industry Publishing House: Beijing, China, 1981.
58. Duan, S.; Ru, C.; Li, Z.; Wang, M.; Xu, H.; Li, H.; Wu, P.; Zhan, W.; Zhou, J.; Zhao, W.; et al. Reviews of methods for land surface temperature retrieval from Landsat thermal infrared data. *J. Remote Sens.* **2021**, *25*, 1591–1617.
59. Sekertekin, A.; Bonafoni, S. Land Surface Temperature Retrieval from Landsat 5, 7, and 8 over Rural Areas: Assessment of Different Retrieval Algorithms and Emissivity Models and Toolbox Implementation. *Remote Sens.* **2020**, *12*, 294. [[CrossRef](#)]
60. Bonham-Carter, G.F.; Agterberg, F.P.; Wright, D.F. Weight of evidence modeling: A new approach to mapping mineral potential. In *Statistical Applications in the Earth Sciences*; Wiley: Hoboken, NJ, USA, 1989; pp. 171–183.
61. Riisager, P.; Rasmussen, T.M. Aeromagnetic survey in south-eastern Greenland: Project Aeromag 2013. *Geol. Surv. Den. Greenl. Bull.* **2014**, *31*, 63–66. [[CrossRef](#)]
62. Armour-Brown, A.; Tukiainen, T.; Wallin, B. *South Greenland Uranium Exploration Programme; Final Report*; Groenlands Geologiske Undersoegelse: Copenhagen, Denmark, 1982; Volume 14.
63. Xiaoliang, F.; Mingjie, W.; Chengmin, W.E.N.; Huihua, Z. The preliminary study of the exploration potential of the Liwu copper deposit and its surrounding areas, western Sichuan. *Sediment. Geol. Tethyan Geol.* **2007**, *27*, 9–13.
64. Petersen, O.V.; Gault, R.A.; Balic-Zunic, T. Odintsovit from the Ilimaussaq alkaline complex, South Greenland. *Neues Jahrb. Mineral.-Mon.* **2001**, 235–240.
65. Petersen, O.V. List of all minerals identified in the Ilímaussaq alkaline complex, South Greenland. *Geol. Greenl. Surv. Bull.* **2001**, *190*, 25–33. [[CrossRef](#)]
66. Petersen, O.V.; Johnsen, O.; Micheelsen, H.I. Turkestanite from the Ilimaussaq alkaline complex, South Greenland. *Neues Jahrb. Mineral.-Mon.* **1999**, 424–432.
67. Quan, X.; Liu, C.; Zhao, Y. The evaluation of uranium mineral resources potential in Greenland. *Geol. Bull. China* **2019**, *38*, 1071–1079.
68. Peleli, S.; Kouli, M.; Marchese, F.; Lacava, T.; Vallianatos, F.; Tramutoli, V. Monitoring temporal variations in the geothermal activity of Miocene Lesvos volcanic field using remote sensing techniques and MODIS—LST imagery. *Int. J. Appl. Earth Obs. Geoinf.* **2021**, *95*, 102251. [[CrossRef](#)]
69. Hewson, R.; Mshiu, E.; Hecker, C.; van der Werff, H.; van Ruitenbeek, F.; Alkema, D.; van der Meer, F. The application of day and night time ASTER satellite imagery for geothermal and mineral mapping in East Africa. *Int. J. Appl. Earth Obs. Geoinf.* **2020**, *85*, 101991. [[CrossRef](#)]
70. Sanchez-Aparicio, M.; Andres-Anaya, P.; Del Pozo, S.; Lagueta, S. Retrieving Land Surface Temperature from Satellite Imagery with a Novel Combined Strategy. *Remote Sens.* **2020**, *12*, 277. [[CrossRef](#)]

71. Romaguera, M.; Vaughan, R.G.; Ettema, J.; Izquierdo-Verdiguier, E.; Hecker, C.A.; van der Meer, F.D. Detecting geothermal anomalies and evaluating LST geothermal component by combining thermal remote sensing time series and land surface model data. *Remote Sens. Environ.* **2018**, *204*, 534–552. [[CrossRef](#)]
72. Crosta, A.P.; De Souza, C.R.; Azevedo, F.; Brodie, C. Targeting key alteration minerals in epithermal deposits in Patagonia, Argentina, using ASTER imagery and principal component analysis. *Int. J. Remote Sens.* **2003**, *24*, 4233–4240. [[CrossRef](#)]
73. Chen, C.; Leng, C.; Si, G. Comprehensive Metallogenic Prediction Based on GIS and Analytic Hierarchy Process: A Case Study of Kumishi Region in Xinjiang. *Gold Sci. Technol.* **2020**, *28*, 213–227.